Frontiers of Physics
https://doi.org/10.1007/s11467-022-1156-3
Front. Phys.
17(5), 53501 (2022)

RESEARCH ARTICLE

A polarization-sensitive, self-powered, broadband and fast $Ti_3C_2T_x$ MXene photodetector from visible to near-infrared driven by photogalvanic effects

Bo Liu, Liyu Qian, Yanliang Zhao, Yiwen Zhang, Feng Liu, Yi Zhang†, Yiqun Xie‡, Wangzhou Shi

Department of Physics, Shanghai Normal University, Shanghai 200234, China
Corresponding authors. E-mail: †yzhang@shnu.edu.cn, ‡yqxie@shnu.edu.cn
Received September 20, 2021; accepted February 28, 2022

Broadband, self-power, and polarization-sensitivity are desirable qualities for a photodetector. However, currently few photodetectors can fulfill these requirements simultaneously. Here, we propose a $Ti_3C_2T_x$ (MXene) photodetector that is driven by the photogalvanic effect with impressive performances. A polarization-sensitive photocurrent is generated at zero bias under the illumination of linearly polarized laser light of 1064 nm, with an extinction ratio of 1.11. Meanwhile, a fast response with a 32/28 ms rise/decay time and a large on/off switching ratio of 120 are achieved. Besides, a robust zero-bias photocurrent is also generated in the photodetector under the illumination of 940 and 620 nm light, as well as the white light, showing a broadband photoresponse from the near-infrared to visible. Moreover, quantum transport simulations indicate that the photogalvanic effect plays an important role in the generation of the polarized photocurrent at zero bias due to the broken space inversion symmetry of the stacked few-layer $Ti_3C_2T_x$. Our results shed light on a potential application of the $Ti_3C_2T_x$–MXene in the low-power photodetection with high performances.

Keywords photodetection, polarization-sensitivity, photogalvanic effects, $Ti_3C_2T_x$, MXene, quantum transport simulations

1 Introduction

Two-dimensional (2D) materials have shown extraordinary application potential in photodetection because of their excellent electronic, optical, and mechanical properties. Photodetectors based on 2D materials such as graphene [1, 2], transition metal dihalides [3, 4], and hexagonal boron nitride [5] have demonstrated excellent performance. A high-performance photodetector generally possesses one or more features including fast photoresponse [6–8], high quantum efficiency, polarization sensitivity, self-power, low cost, etc. [9–12]. For example, the 2D MoS_2 based photodetector has shown an extremely high detectivity of 9.8×10^{16} cm·Hz$^{1/2}$·W^{-1} [13]. A photodetector based on the 2D $Ga_2In_4S_9$ has shown a strong photoresponsivity of 10^4 A·W^{-1}at 360 nm with a high external quantum efficiency of 3.85×10^4 %. Besides, several photodetectors based on 2D materials have shown a polarization sensitivity, such as GeS_2 [14], GeSe [15], black phosphorus/MoS_2 heterojunction [16], GeSe/MoS_2 van der Waals heterojunction [17], and 2D hybrid perovskite-type ferroelectrics [18, 19]. Particularly, a record high extinction ratio of 112.2 has recently been obtained using the graphene/$PdSe_2$/germanium photodetector for 650 nm light at zero bias [20]. However, such polarization-sensitive photodetectors are usually not self-powered or are composed of complicated heterostructures, which either increase the energy consumption or require an expensive and complex fabrication technique.

In theories, quantum transport simulations have proposed several highly polarization-sensitive 2D photodetectors based on monolayer phosphorene [21], antimonene [22], 2D wide-bandgap material [23], and their heterostructures [24]. These theoretically proposed photodetectors are driven by the photogalvanic effect (PGE), namely, bulk photovoltaic effect [25–29]. This effect is essentially a second-order nonlinear optical response to the electrical field of polarized light and occurs only in materials without space inversion symmetry. It can produce a persistent polarization-sensitive photocurrent at zero bias under the illumination of polarized light, and therefore is attractive for a self-powered and polarization-sensitive photodetection. For example, recent experiments have demonstrated that the PGE driven photodetectors based on the 2D ferroelectric materials showed a high extinction ratio up to 15 [18, 19]. Nevertheless, it is currently

* Special Topic: MXene and Its Applications (Eds.: Qing Huang, Ju Han Lee & Guangcun Shan). This article can also be found at http://journal.hep.com.cn/fop/EN/10.1007/s11467-022-1156-3.

of particular interest to fabricate a photodetector that is broadband, self-powered, polarization-sensitive and low-cost at the same time.

2D MXenes [30–33] have recently attracted wide research attention in optoelectronics [34–36], along with their fascinating potential in energy storage [37] and catalyst [38]. For instance, MXenes [39] have been incorporated in 2D heterostructures including MoS_2 /MXene [40] and Ti_3C_2 MXene/Silicon to enhance optoelectronic properties of a photodetector [41], owing to their good conductivity and high optical transmittance. Recently, photodetectors based on the MXene-perovskite arrays have shown a high responsivity of 84.77 $A{\cdot}W^{-1}$ and a high specific detectivity of 3.22×10^{12} Jones, with a broadband photoresponse from visible to near-infrared [36]. However, photodetectors exclusively based on 2D MXenes have rarely been studied so far.

In this work, we fabricated a kind of $Ti_3C_2T_x$–Mxene photodetector via a low-cost multiple spin-coating method and demonstrated a polarization-sensitive, self-powered, broadband and fast photodetector. A polarization-sensitive photocurrent is produced at a 1064 nm laser light at zero bias, with a good on/off ratio of 1.2×10^2 and a millisecond response time. The generation of the photocurrent is mainly attributed to the photogalvanic effect (PGE) according to quantum transport simulations. Our results, therefore, propose a high-performance $Ti_3C_2T_x$–MXene photodetector and explore the potential of MXenes in photodetection.

2 Experimental section

Materials preparation. Few layers $Ti_3C_2T_x$ MXene were obtained by top-down wet etching of the Ti_3AlC_2 phase (Foshan XinXi technology CO. LTD, 99.8 %, 400 mesh) using LiF/HCl solution. First, mix LiF (1 g, Aladin) and HCl (20 mL, 9 M, Beijing Chemical Factory) samples fully. second, 1 g Ti_3AlC_2 powder was added into the mixed powder and stirred at 30 °C for 48 h. Then, the mixture was centrifuged several times and washed with deionized water to make the PH of the solution neutral. The precipitate was washed with distilled water several times. Finally, $Ti_3C_2T_x$ dispersion solution could be obtained by ultrasonic treatment under the condition of N_2 flow.

Device fabrication. Acetone, ethanol, and deionized water were successively used for ultrasonic cleaning of the Si wafer (thickness: 285–315 μm, type: P, dopant: B, resistivity: 3000–8000 Ω·cm, LIJING KEJI). Then the diluted hydrofluoric acid was used to remove the oxide layer on the surface. Finally, the silicon wafer was hydrophilic treated with oxygen, which was the key factor for the uniform growth of few-layer $Ti_3C_2T_x$. Take a small amount of $Ti_3C_2T_x$ solution and then spin the liquid onto the substrate at 400 rpm 30 s and 1000 rpm 15 s, successively. The spin-coated device was annealed in a nitrogen glove box at 60 °C for 2 hours. After annealing, the device was evaporated with a 100 nm silver electrode to form a good ohmic contact for testing.

Characterization and measurements. The surface topography of the samples was investigated using an atomic force microscope (AFM, Asylum Research MFP-3D, USA). The morphology of the film was measured using a field emission scanning electron microscope (FE-SEM, Hitachi S-4800, Japan). The chemical properties and composition of the samples were measured by X-ray photoelectron spectroscopy (XPS, Thermo Scientific K-Alpha+, USA). The excitation source was Al Kα ray ($h\nu$ = 1486.6 eV, 12 kV). The beam spot size is 400 μm, and the vacuum degree of the analysis chamber was less than 5.0×10^{-7} mbar. X-ray diffraction (XRD, Bruker D8 Focus X, Germany) patterns were recorded by analytical diffractometer using Cu-Kα radiation with $\lambda/4$ = 0.15418 nm. The white light source is simulated sunlight. The laser operators are ZKLASER-MB series. A Keithley 2440 parameter analyzer was used to measure the electrical properties of the devices. The phase-locked amplifier (MFLI, ZKLASER-MB) and optical chopper were used to collect and reduce the noise of the photoelectric signal.

Computational methods. The photocurrent is calculated based on quantum transport theory by using first-principles software Nanodcal. In the numerical calculations, the DZP atomic orbital basis is used to expand all the physical quantities; the exchange and correlation were treated at the level of the generalized gradient approximation (GGA) functional as parameterized by the PBE approximation; atomic cores are determined by the standard norm-conserving nonlocal pseudopotentials, and $16 \times 1 \times 1$ k-points are used. Details are given in supporting information.

3 Results and discussion

Figure 1(a) shows the full XPS spectrum of etched $Ti_3C_2T_x$ flakes. The flakes are mainly composed of Ti, C, and F elements, and the F element is originated from the etching solution. The details of fitting results of C 1s, Ti 2P and F 1s are shown in Fig. S2(Supplementary information). We minimize the presence of O functional groups in the synthesis process. The appearance of O functional groups might increase the resistance of few-layer MXene devices [42, 43]. During the preparation of MXene flakes, we carried out in a nitrogen glove box to isolate oxygen. Then the flakes were dispersed in dimethylformamide solvent to prevent further oxidation instantly [44, 45]. Raman spectrum and XRD diagram of $Ti_3C_2T_x$ are shown in Figs. 1(b, c).

Usually, the peak of MAX phase TiAlC appears at 39°,

but due to the etching of Al atoms, the strong peak of 39° is replaced by the low-intensity peak of 2D $Ti_3C_2T_x$–MXene after exfoliation. The XRD pattern in Fig. 1(c) shows that the 2θ value of $Ti_3C_2T_x$ is low, indicating that the stratification of $Ti_3C_2T_x$ is obvious. Figure 1(b) shows the Raman spectrum test results of $Ti_3C_2T_x$ sheets. The peak of $Ti_3C_2T_x$ is Ti–C vibration. The overlapping peaks of D and G bands of graphite carbon correspond to 1340 and 1570 cm^{-1}. As the samples were kept in the N_2 glove box for a long time, no oxidation peaks of TiO_2 were found during XRD and Raman tests. UV-Vis absorption spectrum shows that the etched $Ti_3C_2T_x$ has a fairly high absorption from visible light to near-infrared, as shown in Fig. 1(d), indicating that the synthesized few-layer MXene is suitable for light detection from visible to near-infrared wavelengths.

According to the AFM test results, the thickness of the Ti_3C_2 sheet is about 2 nm, which is different from the MAX phase, proving that the Al atoms are successfully etched. To better analyze the size distribution of MXene flakes, we calculated the area size of MXene flakes in the measured AFM image of MXene thin films. We randomly selected 11 MXene slices for area measurement, and the average area is 0.12 μm^2 (Fig. S1). Figures 1(f) and (g) are the few-layer Ti_3 C_2 sheets (red region) taken by high-power transmission electron microscopy at different multiples. It can be seen from the figure that the few-layer Ti_3C_2 sheets were successfully etched without the particles of the parent phase. The multi-rings shown in the SAED illustration in Fig. 1(g) prove that the Ti_3C_2 sheet is polycrystalline.

We fabricated four kinds of devices with 2, 4, 6, 8 spins, respectively, which were named Device-2, 4, 6, 8. The thickness of the four devices increases with different spins, ranging from 25 to 150 nm, as shown in Fig. 2(a). Figures 2(b) and (c) show the typical cross-section SEM images of the MXene in Device-2 and Device-8, which exhibit overall uniform films that can facilitate the transport and separation of photo-excited carriers. The optical path diagram and detection instruments are shown in Fig. 2(d). A laser light of 1064 nm transports through the chopper, polarizer, half-wave plate, convergent lens, and finally illuminates on the device surface. A lock-in amplifier is used to reduce the noise of the environment. A source meter is used to control bias and collect the photocurrent. Four electrodes are constructed in a cross-type, as shown in Fig. 2(b), and the photocurrent was measured along the x-direction from electrode 1 to 2, and the y-direction (electrode 3 to 4), respectively. In the following, we mainly present the results measured for the x-direction. All measurements were performed on the same optical platform to ensure the stability of the detection.

We measured the photocurrent within a finite bias range and found that the photocurrent varies linearly with the bias at a small voltage, as shown in Fig. 3(a). Remarkably, a robust photocurrent is produced at zero bias for all four devices, indicating a self-powered operation mode. This zero-bias photocurrent increases from 10^{-7} to 10^{-6} A with

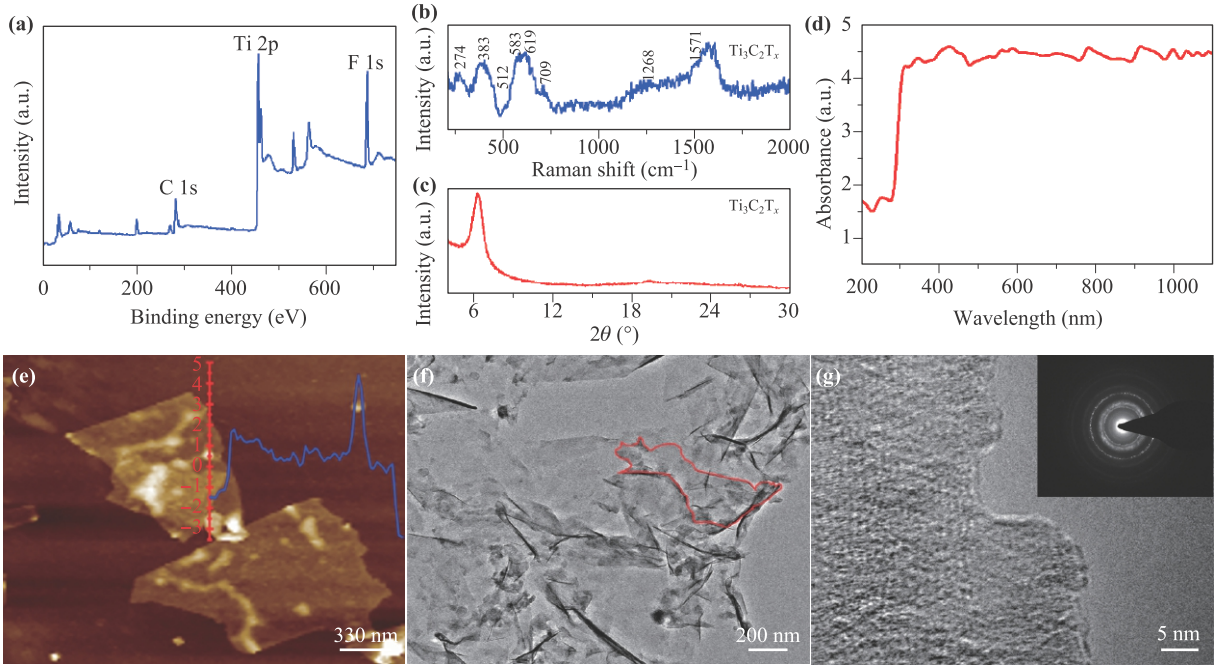

Fig. 1 **(a)** XPS survey spectrum of synthesized $Ti_3C_2T_x$, **(b)** Raman spectrum, **(c)** X-ray diffraction, and **(d)** UV-Vis absorption spectrum of synthesized $Ti_3C_2T_x$. **(e)** AFM, **(f)** TEM, and **(g)** HRTEM surface topography of synthesized $Ti_3C_2T_x$. The inset of (g) is the corresponding SAED pattern.

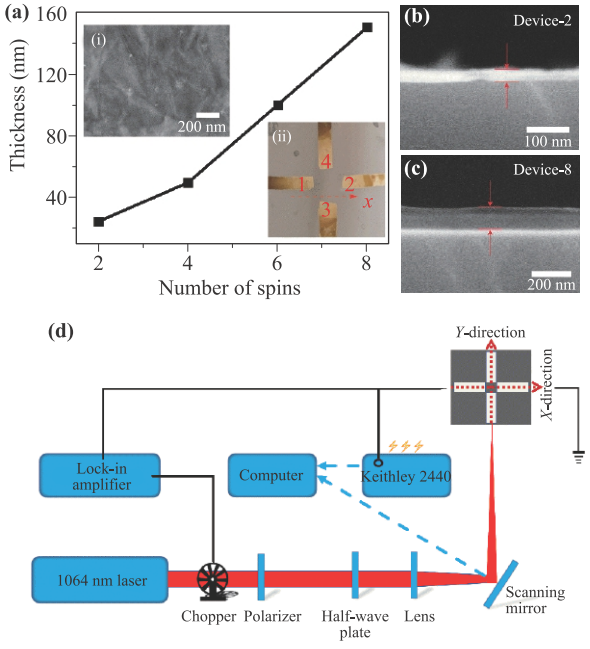

Fig. 2 **(a)** Thickness of the device for different spins. Inset (i) is the SEM surface topography of the $Ti_3C_2T_x$ and inset (ii) is the device with four electrodes. **(b, c)** are the SEM cross-sections of the $Ti_3C_2T_x$ photodetectors. **(d)** is the diagram of light paths and detection instruments.

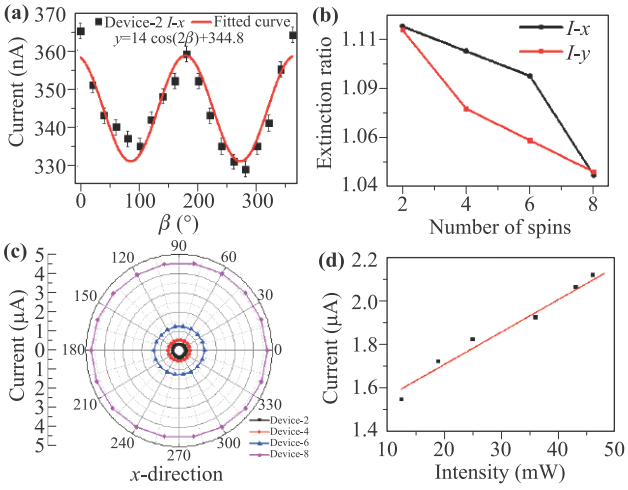

Fig. 4 **(a)** Variation of the current with the polarization angle β for a 1064 nm linearly polarized laser light. (The red line is the fitting curve.) **(b)** The extinction ratio of the four devices with different spins was measured in the x-direction and y-direction. **(c)** The corresponding photocurrents depend on the incident light polarization for Device-2 at 1064 nm and zero-bias. **(d)** The dependence of current on the power intensity.

the number of the increasing spins, as shown in Fig. 3(b). The switching efficiency was then evaluated from the time-dependent periodical signal in Fig. 3(b). We obtained a good on/off ratio, which increases with spins and reaches the maximum of 120 for Device-8, as shown in Fig. 3(c). Moreover, all devices show a very fast photoresponse, as shown in Fig. 3(d). For example, Device-8 has a fast rise/decay time of 32/28 ms. In all, these results show that this sample has the largest photocurrent and photoresponsivity. This is mainly ascribed to the increased optical absorption due to its thicker layers than the other three devices, as the $Ti_3C_2T_x$ has a high transmittance [46].

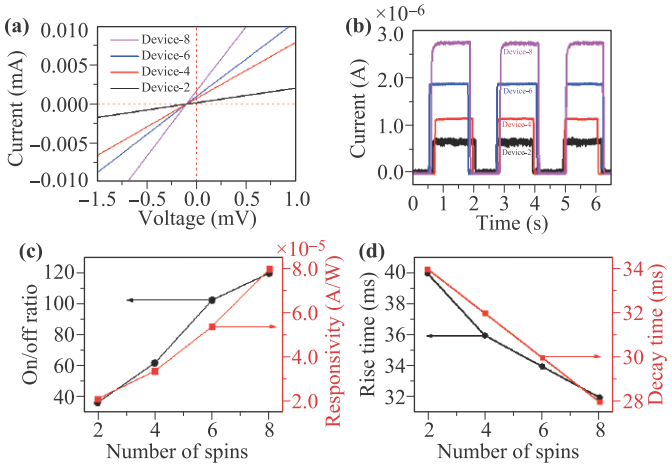

Fig. 3 **(a)** I–V curves and **(b)** the time-resolved photoresponse of the four devices with different spins under the 1064 nm laser light. **(c)** On/off ratio and responsivity of the four devices, and **(d)** the rise and decay time of the devices at zero bias.

Moreover, we found that the photocurrent is polarization sensitive, as shown in Fig. 4(a). By changing the polarization angle of the laser light, the photocurrent has a cosine dependence on the polarization angle β, which can be well fitted by a function $14\cos(2\beta) + 344.8$, as indicated by the red solid line in Fig. 4(a). The Polarization-dependent current of the four devices along the x- and y-directions at 1064 nm are given in figures S3 and S4. To evaluate the polarization sensitivity, we define an extinction ratio as I_{max}/I_{min}, and show it in Fig. 4(b) for the four devices. The extinction ratio decreases monotonously with the number of increasing spins. The largest value is 1.11 obtained for Device-2 with 2 spins. Figure 4(c) shows the polarization-dependent photocurrent for the four devices, respectively. In addition, the photocurrent has a linear dependence on the laser power, as shown in Fig. 4(d).

The photodetectors also have a robust zero-bias photoresponse to the 940 and 620 nm, as well as white light generated from an ordinary light source, as shown in Fig. 5. A fast photoresponse was also obtained, with the rise/decay time of the order of 10^2 ms.

The above results show that the photodetectors based on the 2D $Ti_3C_2T_x$–MXene simultaneously have a self-powered, polarization-sensitive, fast, and broadband pho-

toresponse from the near-infrared to visible. The photodetectors are built with only 2D $Ti_3C_2T_x$ spins using the spin-coating method on silicon, which is a simple and low-cost experimental method. It does not rely on any expensive equipment (used to fabricate heterojunction) and can prepare MXene films with high quality and excellent performance on a variety of substrates. Given that studies on photodetectors based on 2D Mxenes are currently very limited, the proposed 2D $Ti_3C_2T_x$–photodetectors in this work give an insight into potential applications of 2D MXenes in high-performance photodetection.

Next, we analyze a possible mechanism that is responsible for the self-powered and polarization-sensitive photocurrent generated in the $Ti_3C_2T_x$–photodetectors. The photodetector contains several spins of $Ti_3C_2T_x$, which is stacked by few-layers MXene flakes. There exits inevitably mismatch, dislocation, and overlapping between layers and spins, which breaks the space inversion symmetry of the pristine 2D $Ti_3C_2T_x$ [47]. Therefore, the linear PGE can be induced under the illumination of linearly polarized light. The PGE photocurrent is generated without the need for any electrical fields (zero bias) and has a cosine dependence on the polarization angle determined by the symmetry, as well as a linear dependence on the light power. All these characteristics have been observed in our experimental results. This indicates that the PGE has an important contribution to the photocurrent in our photodetectors. Therefore, we construct a device model for the $Ti_3C_2T_x$ photodetectors and calculate the photocurrent for linearly polarized light, based on quantum transport simulations by using the first-principles package Nanodcal [48]. We considered two possible surface terminations –OH and –F in the calculations. To mimic the broken space inversion symmetry of the device, we construct a bilayer $Ti_3C_2T_x$ photodetector with a lateral

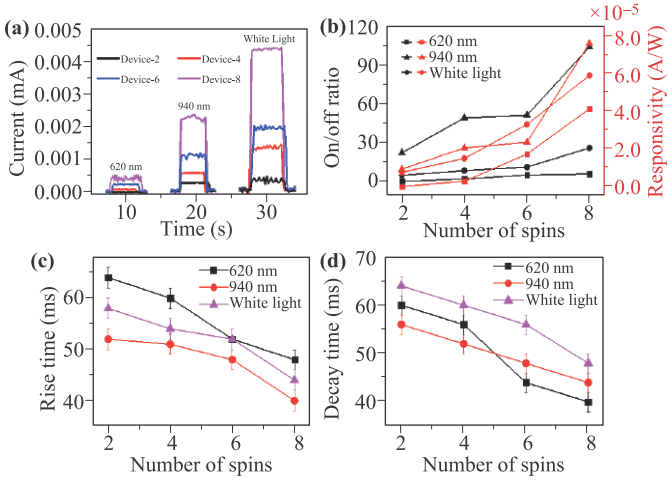

Fig. 5 **(a)** A time-resolved photocurrent of the three devices with the different spins under the 620 nm, 940 nm, and white light at zero bias. **(b)** On/off ratio and responsivity, **(c)** the rise, and **(d)** decay time.

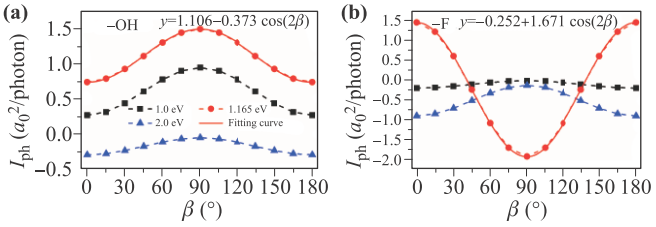

Fig. 6 Photocurrent of the OH- and F-terminated bilayer $Ti_3C_2T_x$ photodetector at 1.0, 1.165, and 2.0 eV for different polarization angle β.

shift between the top and bottom layers to obtain a C_s symmetry, whereby a PGE photocurrent can be generated at zero bias under the illumination of linearly polarized light. (Details of the model and calculation methods are presented in supporting information.)

The photocurrent (I_{ph}) is calculated for linear polarized light with three different photon energies of 1.0 eV (1240 nm), 1.165 eV (1064 nm) and 2.0 eV (620 nm) at a zero bias, as shown in Fig. 6. It can be seen that the photocurrent has an evident cosine dependence on the polarization angle with a form $\cos(2\beta)$. For the OH-terminated photodetector, the extinction ratios are 3.50, 2.02, and 5.80, respectively. The extinction ratios are 7.0, 1.35, and 6.21 for the F-terminated photodetector, respectively. These extinction ratios are relatively higher than that of the experimental value. A possible reason is that there is no dark current in our calculations, which can reduce the extinction ratio in real experiments. Nevertheless, these simulation results also present a zero-bias, broadband, and polarization-sensitive photocurrent, showing a good qualitative agreement with the experimental results. This indicates that the PGE has an important contribution to the high performance of the 2D $Ti_3C_2T_x$ photodetector, which has a broken space inversion symmetry. In a recent experiment, the PGE is also the dominant mechanism for an anisotropic ultrasensitive $PdTe_2$-based phototransistor for room-temperature long-wavelength detection [49].

4 Conclusion

In summary, we have fabricated the 2D $Ti_3C_2T_x$–MXene using the spin-coating method and built photodetectors with different spins. The robust photocurrent is generated at zero bias in a broadband range from the near-infrared to visible. A fast photoresponse and a high switching ratio are obtained for the 1064 nm laser light. The photocurrent also shows an evident polarization sensitivity with a 1.11 extinction ratio. Quantum transport simulations indicate that the PGE has an important contribution to the generation of the photocurrent. Our results propose a high-performance $Ti_3C_2T_x$–Mxene photodetector that possesses simultaneously a self-powered, polarization-

sensitive, broadband, and fast photoresponse. It also sheds light on the potentials of MXenes in a low-power photodetection.

Electronic supplementary materials are available in the online version of this article at https://doi.org/10.1007/s11467-022-1156-3 and https://journal.hep.com.cn/fop/EN/10.1007/s11467-022-1156-3 and are accessible for authorized users.

Acknowledgements This work was supported by the National Natural Science Foundation of China (Grant Nos. 12073018, 51871156, U2031128, and 61904107), the State Key Program of National Natural Science of China (No. U1931205), and Shanghai Natural Science Foundation (No. 22ZR1446100).

References

1. F. I. Alzakia, B. S. Tang, S. J. Pennycook, and S. C. Tan, Engineering the photoresponse of liquid-exfoliated 2D materials by size selection and controlled mixing for an ultrasensitive and ultraresponsive photodetector, *Mater. Horiz.* 7(12), 3325 (2020)
2. M. D. Stoller, S. J. Park, Y. W. Zhu, J. H. An, and R. S. Ruoff, Graphene-based ultracapacitors, *Nano Lett.* 8(10), 3498 (2008)
3. Q. H. Wang, K. Kalantar-Zadeh, A. Kis, J. N. Coleman, and M. S. Strano, Electronics and optoelectronics of two-dimensional transition metal dichalcogenides, *Nat. Nanotechnol.* 7(11), 699 (2012)
4. M. Chhowalla, H. S. Shin, G. Eda, L. J. Li, K. P. Loh, and H. Zhang, The chemistry of two-dimensional layered transition metal dichalcogenide nanosheets, *Nat. Chem.* 5(4), 263 (2013)
5. L. Song, L. J. Ci, H. Lu, P. B. Sorokin, C. H. Jin, J. Ni, A. G. Kvashnin, D. G. Kvashnin, J. Lou, B. I. Yakobson, and P. M. Ajayan, Large scale growth and characterization of atomic hexagonal boron nitride layers, *Nano Lett.* 10(8), 3209 (2010)
6. A. A. Hussain, Constructing caesium-based lead-free perovskite photodetector enabling self-powered operation with extended spectral response, *ACS Appl. Mater. Interfaces* 12(41), 46317 (2020)
7. S. Qiao, Y. Liu, J. H. Liu, G. S. Fu, and S. F. Wang, High-responsivity, fast, and self-powered narrowband perovskite heterojunction photodetectors with a tunable response range in the visible and near-infrared region, *ACS Appl. Mater. Interfaces* 13(29), 34625 (2021)
8. H. Kan, W. Zheng, R. C. Lin, M. Li, C. Fu, H. B. Sun, M. Dong, C. H. Xu, J. T. Luo, Y. Q. Fu, and F. Huang, Ultrafast photovoltaic-type deep ultraviolet photodetectors using hybrid zero-/two-dimensional heterojunctions, *ACS Appl. Mater. Interfaces* 11(8), 8412 (2019)
9. X. T. Zhang, X. M. Yao, Z. Y. Li, C. Zhou, X. M. Yuan, Z. Tang, W. D. Hu, X. T. Gan, J. Zou, P. P. Chen, and W. Lu, Surface-states-modulated high-performance InAs nanowire phototransistor, *J. Phys. Chem. Lett.* 11(15), 6413 (2020)
10. X. T. Zhang, H. Huang, X. M. Yao, Z. Y. Lo, C. Zhou, X. Zhang, P. P. Chen, L. Fu, X. H. Zhou, J. L. Wang, W. D. Hu, W. Lu, J. Zou, H. H. Tan, and C. Jagadish, Ultrasensitive mid-wavelength infrared photodetection based on a single In As nanowire, *ACS Nano* 13(3), 3492 (2019)
11. C. Guo, Y. B. Hu, G. Chen, D. C. Wei, L. B. Zhang, Z. Q. Z. Chen, W. L. Guo, H. Xu, C. N. Kuo, C. S. Lue, X. Y. Bo, X. G. Wan, L. Wang, A. Politano, X. S. Chen, and W. Lu, Anisotropic ultrasensitive $PdTe_2$-based phototransistor for room-temperature long-wavelength detection, *Sci. Adv.* 6(36), eabb6500 (2020)
12. L. Tong, X. Y. Huang, P. Wang, L. Ye, M. Peng, L. C. An, Q. D. Sun, Y. Zhang, G. M. Yang, Z. Li, F. Zhong, F. Wang, Y. X. Wang, M. Motlag, W. Z. Wu, G. J. Cheng, and W. D. Hu, Stable mid-infrared polarization imaging based on quasi-2D tellurium at room temperature, *Nat. Commun.* 11(1), 2308 (2020)
13. S. Feng, C. Liu, Q. B. Zhu, X. Su, W. W. Qian, Y. Sun, C. X. Wang, B. Li, M. L. Chen, L. Chen, W. Chen, L. L. Zhang, C. Zhen, F. J. Wang, W. C. Ren, L. C. Yin, X. M. Wang, H. M. Cheng, and D. M. Sun, An ultrasensitive molybdenum-based double-heterojunction phototransistor, *Nat. Commun.* 12(1), 4094 (2021)
14. Y. S. Yang, S. C. Liu, W. Yang, Z. B. Li, Y. Wang, X. Wang, S. S. Zhang, Y. Zhang, M. S. Long, G. M. Zhang, D. J. Xue, J. S. Hu, and L. J. Wan, Air-stable in-plane anisotropic $GeSe_2$ for highly polarization-sensitive photodetection in short wave region, *J. Am. Chem. Soc.* 140(11), 4150 (2018)
15. J. Bullock, M. Amani, J. Cho, Y. Z. Chen, G. H. Ahn, V. Adinolfi, V. R. Shrestha, Y. Gao, K. B. Crozier, Y. L. Chueh, and A. Javey, Polarization-resolved black phosphorus/molybdenum disulfide mid-wave infrared photodiodes with high detectivity at room temperature, *Nat. Photonics* 12(10), 601 (2018)
16. Y. Xin, X. X. Wang, Z. Chen, D. Weller, Y. Y. Wang, L. J. Shi, X. Ma, C. J. Ding, W. Li, S. Guo, and R. B. Liu, Polarization-sensitive self-powered type-II GeSe/Mo S_2 Van Der Waals heterojunction photodetector, *ACS Appl. Mater. Interfaces* 12(13), 15406 (2020)
17. C. M. Ji, D. Dey, Y. Peng, X. T. Liu, L. N. Li, and J. H. Luo, Ferroelectricity-driven self-powered ultraviolet photodetection with strong polarization sensitivity in a two-dimensional halide hybrid perovskite, *Angew. Chem. Int. Ed.* 59(43), 18933 (2020)
18. Y. Peng, X. T. Liu, Z. H. Sun, C. M. Ji, L. N. Li, Z. Y. Wu, S. S. Wang, Y. P. Yao, M. C. Hong, and J. H. Luo, Exploiting the bulk photovoltaic effect in a 2D trilayered hybrid ferroelectric for highly sensitive polarized light detection, *Angew. Chem. Int. Ed.* 59(10), 3933 (2020)
19. D. Wu, J. W. Guo, J. Du, C. X. Xia, L. H. Zeng, Y. Z. Tian, Z. F. Shi, Y. T. Tian, X. J. Li, Y. H. Tsang, and J. S. Jie, Highly polarization-sensitive, broadband, self-powered photodetector based on graphene/$PdSe_2$/germanium heterojunction, *ACS Nano* 13(9), 9907 (2019)
20. Y. Q. Xie, L. Zhang, Y. Zhu, L. Liu, and H. Guo, Photogalvanic effect in monolayer black phosphorus, *Nanotechnology* 26(45), 455202 (2015)

21. F. H. Chu, M. Y. Chen, Y. Wang, Y. Q. Xie, B. Y. Liu, Y. H. Yang, X. T. An, and Y. Z. Zhang, A highly polarization sensitive antimonene photodetector with a broadband photoresponse and strong anisotropy, *J. Mater. Chem. C* 6(10), 2509 (2018)
22. Y. S. Yang, S. C. Liu, X. Wang, Z. B. Li, Y. Zhang, G. M. Zhang, D. J. Xue, and J. S. Hu, Polarization-sensitive ultraviolet photodetection of anisotropic 2D GeS_2, *Adv. Funct. Mater.* 29(16), 1900411 (2019)
23. Y. Z. Luo, Y. B. Hu, and Y. Q. Xie, Highly polarization-sensitive, visible-blind and self-powered ultraviolet photodetection based on two-dimensional wide bandgap semiconductors: A theoretical prediction, *J. Mater. Chem. A* 7(48), 27503 (2019)
24. L. Y. Qian, J. Zhao, and Y. Q. Xie, Enhanced photogalvanic effect in the two-dimensional $MgCl_2/ZnBr_2$ vertical heterojunction by inhomogenous tensile stress, *Front. Phys.* 17(1), 13502 (2022)
25. V. Belinicher and B. I. Sturman, The photogalvanic effect in media lacking a center of symmetry, *Sov. Phys. Usp.* 23(3), 199 (1980)
26. S. M. Young, F. Zheng, and A. M. Rappe, First-principles calculation of the bulk photovoltaic effect in bismuth ferrite, *Phys. Rev. Lett.* 109(23), 236601 (2012)
27. U. Bajpai, B. S. Popescu, P. Plechac, B. K. Nikolić, L. Torres, H. Ishizuka, and N. Nagaosa, Spatio-temporal dynamics of shift current quantum pumping by femtosecond light pulse, *J. Phys. Mater.* 2(2), 025004 (2019)
28. S. Hubmann, G. V. Budkin, M. Otteneder, D. But, D. Sacre, I. Yahniuk, K. Diendorfer, V. V. Bel'kov, D. A. Kozlov, N. N. Mikhailov, S. A. Dvoretsky, V. S. Varavin, V. G. Remesnik, S. A. Tarasenko, W. Knap, and S. D. Ganichev, Symmetry breaking and circular photogalvanic effect in epitaxial $Cd_xHg_{1-x}Te$ films, *Phys. Rev. Mater.* 4(4), 043607 (2020)
29. Y. Z. Luo, Y. Q. Xie, J. Zhao, Y. B. Hu, X. Ye, and S. H. Ke, Perfect in-plane CrI_3 spin-valve driven by photogalvanic effect, *Phys. Rev. Mater.* 5(5), 054004 (2021)
30. L. F. Gao, W. L. Bao, A. V. Kuklin, S. Mei, H. Zhang, and H. Agren, Hetero–MXenes: Theory, synthesis, and emerging applications, *Adv. Mater.* 33(10), 2004129 (2021)
31. S. Y. Pang, Y. T. Wong, S. G. Yuan, Y. Liu, M. K. Tsang, Z. B. Yang, H. T. Huang, W. T. Wong, and J. H. Hao, Universal strategy for HF-free facile and rapid synthesis of two-dimensional MXenes as multifunctional energy materials, *J. Am. Chem. Soc.* 141(24), 9610 (2019)
32. K. J. Griffith, M. A. Hope, P. J. Reeves, M. Anayee, Y. Gogotsi, and C. P. Grey, Bulk and surface chemistry of the niobium MAX and MXene phases from multinuclear solid-state NMR spectroscopy, *J. Am. Chem. Soc.* 142(44), 18924 (2020)
33. J. Y. Sui, X. F. Chen, Y. Li, W. C. Peng, F. B. Zhang, and X. B. Fan, MXene derivatives: Synthesis and applications in energy convention and storage, *RSC Adv.* 11(26), 16065 (2021)
34. J. X. Chen, Z. L. Li, F. L. Ni, W. X. Ouyang, and X. S. Fang, Bio-inspired transparent MXene electrodes for flexible UV photodetectors, *Mater. Horiz.* 7(7), 1828 (2020)
35. S. Chertopalov and V. N. Mochalin, Environment-sensitive photoresponse of spontaneously partially oxidized Ti_3C_2 MXene thin films, *ACS Nano* 12(6), 6109 (2018)
36. A. B. Ren, J. H. Zou, H. G. Lai, Y. X. Huang, L. M. Yuan, H. Xu, K. Shen, H. Wang, S. Y. Wei, Y. F. Wang, X. Hao, J. Q. Zhang, D. W. Zhao, J. Wu, and Z. M. Wang, Direct laser-patterned MXene-perovskite image sensor arrays for visible-near infrared photodetection, *Mater. Horiz.* 7(7), 1901 (2020)
37. S. L. Zhang and W. Q. Han, Recent advances in MXenes and their composites in lithium/sodium batteries from the viewpoints of components and interlayer engineering, *Phys. Chem. Chem. Phys.* 22(29), 16482 (2020)
38. H. T. Chen, A. D. Handoko, T. S. Wang, J. L. Qu, J. W. Xiao, X. P. Liu, D. Legut, Z. W. Seh, and Q. F. Zhang, Defect-enhanced CO_2 reduction catalytic performance in O-terminated MXenes, *Chemsuschem* 13(21), 5690 (2020)
39. J. C. Lei, X. Zhang, and Z. Zhou, Recent advances in MXene: Preparation, properties, and applications, *Front. Phys.* 10(3), 276 (2015)
40. J. T. Zhu, H. Wang, L. Ma, and G. F. Zou, Observation of ambipolar photoresponse from 2D MoS_2/MXene heterostructure, *Nano Res.* 14, 3416 (2021)
41. W. X. Huo, Z. A. Zhang, Z. L. Wang, Z. Y. Wu, J. M. Li, Y. Chai, and X. Huang, Large-area transient conductive films obtained through photonic sintering of 2D materials, *Adv. Mater. Technol.* 7(2), 2100439 (2021)
42. X. H. Zha, K. Luo, Q. W. Li, Q. Huang, J. He, X. D. Wen, and S. Y. Du, Role of the surface effect on the structural, electronic and mechanical properties of the carbide MXenes, *Europhys. Lett.* 111(2), 26007 (2015)
43. G. R. Berdiyorov, Effect of surface functionalization on the electronic transport properties of Ti_3C_2 MXene, *Europhys. Lett.* 111(6), 67002 (2015)
44. O. Mashtalir, M. Naguib, V. N. Mochalin, Y. Dall'Agnese, M. Heon, M. W. Barsoum, and Y. Gogotsi, Intercalation and delamination of layered carbides and carbonitrides, *Nat. Commun.* 4(1), 1716 (2013)
45. K. Maleski, V. N. Mochalin, and Y. Gogotsi, Dispersions of two-dimensional titanium carbide MXene in organic solvents, *Chem. Mater.* 29(4), 1632 (2017)
46. Q. Zou, W. Y. Guo, L. Zhang, L. T. Yang, Z. Y. Zhao, F. Liu, X. Ye, Y. Zhang, and W. Z. Shi, MXene-based ultrathin film for terahertz radiation shielding, *Nanotechnology* 31(50), 505710 (2020)
47. Q. Kong, X. An, L. Huang, X. Wang, W. Feng, S. Qiu, Q. Wang, and C. Sun, A DFT study of $Ti_3C_2O_2$ MXenes quantum dots supported on single layer graphene: Electronic structure a hydrogen evolution performance, *Front. Phys.* 16(5), 1 (2021)
48. J. Taylor, H. Guo, and J. Wang, *Ab initio* modeling of quantum transport properties of molecular electronic devices, *Phys. Rev. B* 63(24), 245407 (2001)
49. C. Guo, Y. Hu, G. Chen, D. Wei, L. Zhang, Z. Chen, W. Guo, H. Xu, C. N. Kuo, C. S. Lue, X. Bo, X. Wan, L. Wang, A. Politano, X. Chen, and W. Lu, Anisotropic ultrasensitive $PdTe_2$-based phototransistor for room-temperature long-wavelength detection, *Sci. Adv.* 6(36), eabb6500 (2020)